

# A superconducting half-dome in bilayer nickelates

Yidi Liu<sup>1,2\*†</sup>, Bai Yang Wang<sup>1,3\*‡</sup>, Jiarui Li<sup>1,3</sup>, Yaoju Tarn<sup>1,3</sup>, Lopa Bhatt<sup>4</sup>, Michael Colletta<sup>4</sup>, Yi-Ming Wu<sup>1,2</sup>, Cheng-Tai Kuo<sup>5</sup>, Jun-Sik Lee<sup>5</sup>, Berit H. Goodge<sup>6</sup>, David A. Muller<sup>4,7</sup>, Zhi-Xun Shen<sup>1,2,3,8</sup>, Srinivas Raghu<sup>1,2,8</sup>, Harold Y. Hwang<sup>1,3,8§</sup>, and Yijun Yu<sup>1,3,9¶</sup>

<sup>1</sup>Stanford Institute for Materials and Energy Sciences, SLAC National Accelerator Laboratory, Menlo Park, CA 94025, USA

<sup>2</sup>Department of Physics, Stanford University, Stanford, CA 94305, USA

<sup>3</sup>Department of Applied Physics, Stanford University, Stanford, CA 94305, USA

<sup>4</sup>School of Applied and Engineering Physics, Cornell University, Ithaca, New York 14850, USA

<sup>5</sup>Stanford Synchrotron Radiation Lightsource, SLAC National Accelerator Laboratory, Menlo Park, CA, USA

<sup>6</sup>Max Planck Institute for Chemical Physics of Solids, 01187 Dresden, Germany

<sup>7</sup>Kavli Institute at Cornell for Nanoscale Technology, Cornell University, Ithaca, New York 14850, USA

<sup>8</sup>Geballe Laboratory for Advanced Materials, Stanford University, Stanford CA, USA

<sup>9</sup>State Key Laboratory of Surface Physics and Department of Physics, Fudan University, Shanghai, China

\*These authors contributed equally to this work

†Contact Author: [yidil@stanford.edu](mailto:yidil@stanford.edu)

‡Contact Author: [bwang87@stanford.edu](mailto:bwang87@stanford.edu)

§Contact Author: [hyhwang@stanford.edu](mailto:hyhwang@stanford.edu)

¶Contact Author: [yuyijun@fudan.edu.cn](mailto:yuyijun@fudan.edu.cn)

Understanding how superconductivity emerges and collapses in correlated electron systems remains a central challenge in condensed matter physics. As a recently discovered member of the high temperature superconductor family, bilayer nickelates provide a new opportunity for examining this problem. Their pronounced sensitivity to oxygen stoichiometry, while posing challenges for stabilizing superconductivity, simultaneously offers an effective control parameter for tuning electronic phases. Here we report a superconducting half-dome in compressively strained bilayer nickelate thin films as a function of continuous tuning of oxygen stoichiometry. Starting from an optimally superconducting state, increasing oxygen stoichiometry gradually suppresses superconductivity toward a metallic phase, whereas decreasing oxygen stoichiometry drives a granular superconductor-to-insulator transition while leaving the superconducting onset intact. This half-dome structure can be understood to arise from the contrasting roles played by interstitial oxygen versus oxygen vacancies – namely the dominance of doping versus scattering. Notably, the half-dome emerges consistently across samples with different rare-earth combinations, with or without alkaline-earth doping, revealing a general feature of the bilayer nickelate phase diagram.

## I. INTRODUCTION

Establishing a generic phase diagram has been central in the study of high temperature superconductors across various materials families [1,2]. Such diagrams uncover the interplay between competing ground states, provide a unifying framework connecting disparate experimental observations, and guide the understanding of materials-related parameters. Comparing phase diagrams across different superconducting families further highlights universal features of high temperature superconductivity. Such an endeavor is now underway in the bilayer nickelates.

Since the discovery of superconductivity in bulk and thin film bilayer nickelates [3–7], their superconducting phase diagram has been explored along various dimensions including pressure [3–5,8–11], strain [6,7,12–15], oxygen stoichiometry [16–20], and substitutional hole doping [21]. For bulk samples, superconductivity is found to be broadly robust to variations in pressure above a threshold value, yet

sensitive to oxygen off-stoichiometry [22–26] and crystal symmetry [27]. In thin films, a hole-doping-dependent superconducting dome is reported, with the optimal superconductivity transition temperature ( $T_c$ ) observed at a finite doping level [21]. Superconductivity in thin films is also seen to positively correlate with compressive epitaxial strain [15] and pressure [14].

Bridging these disparate, partial phase diagrams and constructing a coherent view of superconductivity in bilayer nickelates is a high priority. Our work is motivated to unify aspects of the high-dimensional phase space of strain (or pressure), substitutional (Ca) hole doping, and oxygen stoichiometry. By examining thin film bilayer nickelates systematically across oxygen stoichiometry and substitutional doping, we find a universal superconducting half-dome, governed by oxygen stoichiometry in samples across different chemical doping levels, as summarized in Fig. 1. Oxygen stoichiometry exhibits two qualitatively distinct manifestations in bilayer nickelates. Excess

oxygen predominantly acts as an electronic tuning parameter, modifying carrier density via interstitial doping while gradually weakening superconductivity. In contrast, oxygen deficiency rapidly introduces strong scattering and electronic inhomogeneity, suppressing coherent metallic transport while preserving local superconducting fluctuations, consistent with granular superconductivity [28]. This pronounced asymmetry suggests that oxygen vacancies play a fundamentally different role from oxygen interstitials, reflecting the electronic fragility of the  $\text{NiO}_2$  bilayer units, where apical and planar oxygen coordination is intimately tied to inter- and intra-layer coupling. In the following we present the experimental results that establish this phase diagram.

The starting point for this study is the realization that high crystallinity and oxygen stoichiometry are prerequisites for optimizing superconductivity in bilayer nickelate films [23]. Going beyond optimization, we see a trend in ozone-density [ $w(\text{O}_3)$ ] versus annealing-temperature ( $T_{\text{anneal}}$ ) that systematically varies  $T_c$ , as shown in Fig. 2(a). Notably, samples annealed closer to (but not beyond) the boundary between the bilayer phase and higher-order RP phases exhibit systematically reduced  $T_c$ , as reflected by the size of the filled circles (which is plotted proportional to  $T_c$ ). We observe this trend in two different variations of bilayer nickelates,  $\text{La}_2\text{PrNi}_2\text{O}_{7+\delta}$  (LPNO, Fig. 2(b)) and  $\text{La}_2\text{SmNi}_2\text{O}_{7+\delta}$  (LSNO, Fig. 2(c)). We note that  $\delta$  may take either positive or negative values throughout this manuscript corresponding to oxygen excess or deficiency, respectively. Importantly, the reduction in  $T_c$  is not accompanied by a structural transformation into higher-order RP phases (Fig. S1). This provides strong evidence that superconductivity is also influenced by the evolution of oxygen stoichiometry within the stable bilayer phase (a similar trend also observed in ref. [20]).

## II. RESULTS

### A. Excess oxygen in metallic bilayer nickelate thin films

While  $\text{La}_2\text{NiO}_{4+\delta}$  is known to accommodate interstitial excess oxygen [29], initial studies of bulk bilayer nickelates reported a clear tendency toward apical oxygen vacancies [22,30]. Given that the bilayer nickelate structure incorporates both perovskite and rock-salt building blocks, it can host either oxygen deficiency or oxygen excess. Indeed, recent studies show evidence of interstitial oxygen for both bulk and thin film bilayer nickelates [24–26,31]. Thus, we deduce that the suppression of superconductivity in samples undergoing more oxidizing ozone annealing conditions in Fig. 2 arises from excess oxygen intercalation.

Directly probing oxygen content in thin films is

challenging, and currently impossible at the required accuracy for these ultrathin films whose thickness is limited to the regime of coherent strain. Unlike bulk cuprates [32] or nickelates [10,11], where thermogravimetric analysis or chemical titration can accurately determine the oxygen content, only a limited set of techniques can be applied here; we use spectroscopy to probe the evolution of the oxygen stoichiometry by comparison to bulk data.

First, we establish a correspondence between an optimally superconducting LPNO film (identified through transport) and its oxygen stoichiometry. Specifically, ‘optimally superconducting’ refers to samples with  $T_{c,\text{onset}} > 40$  K and a narrow transition width (i.e.  $T_{c,90\%} - T_{c,10\%} < 10$  K; the various criteria used to define  $T_c$  throughout the manuscript are illustrated in Fig. S2) just after ozone annealing. Electron energy-loss spectroscopy (EELS) was performed on such an LPNO sample for comparison to bulk reference data correlating the O  $K$ -edge pre-peak intensity with oxygen stoichiometry [22,25] (Fig. 3(a)). The specimen was prepared by cryogenic focused ion beam (cryo-FIB) to eliminate processing-induced modification of the oxygen stoichiometry (see Methods), and spectra were spatially averaged over the bottom half of the film to exclude measurements of possible oxygen loss near the surface. The measured pre-peak intensity aligns with the  $\delta \approx 0$  reference bulk sample (Fig. 3(a)), indicating that optimally superconducting samples are (spectroscopically) very similar to the stoichiometric composition  $\text{La}_2\text{PrNi}_2\text{O}_7$ . By analogy, we infer that stoichiometric  $\text{La}_2\text{SmNi}_2\text{O}_7$  samples also possess optimal superconducting properties, given that the optimal superconducting LSNO films have similar metrics of  $T_c$  and Hall coefficient ( $R_H$ ) to those of the LPNO counterparts.

Next, we examine the X-ray absorption spectra (XAS) of samples subjected to different oxygen-treatment conditions, which show different transport behaviors. In Fig. 3(b), three LSNO samples are shown: an insulating sample (as-grown, oxygen-deficient), an optimally superconducting sample (stoichiometric, as argued above), and a non-superconducting metallic sample (after ozone annealing near the phase boundary in Fig. 2(a), oxygen-rich). Ni  $L_2$ -edge XAS evolves from the  $\text{Ni}^{2+}$ -like spectrum in the oxygen-deficient sample to more  $\text{Ni}^{3+}$ -like spectrum in the oxygen-rich sample (Fig. 3(c)), consistent with expectations from formal electron counting. This trend is further illustrated by O  $K$ -edge XAS spectra in Fig. 3(d), where the oxygen pre-peak intensity increases from the insulating sample to the optimally superconducting sample and finally to the non-superconducting metallic sample, indicating a systematic increase in oxygen content. Such changes in oxygen stoichiometry are also

accompanied by subtle structural changes, including a slight difference in the  $c$ -lattice constant. However, conflicting reports of the  $c$ -dependence on oxygen stoichiometry exist in the literature for both bulk and thin films. A detailed discussion is in Fig. S3.

Before closing this section, several observations are noteworthy: (i) Similar to bulk results [11], LSNO films consistently exhibit better crystallinity than LPNO. (ii) This, in turn, allows LSNO films to approach the phase boundary more closely without transforming into mixed higher-order RP phases and, as a result, these specimens intercalate more oxygen and exhibit a lower  $T_c$  as shown in Fig. 2(b)-(c). In the extreme cases, superconductivity disappears. (iii) A lower residual resistance ratio (RRR, defined as  $\rho(200\text{K})/\rho(60\text{K})$ ) is observed in samples with lower  $T_c$ , suggesting slightly increased scattering.

### B. Evolution of superconductivity with oxygen stoichiometry in LSNO

Having benchmarked oxygen stoichiometry for discrete samples spanning the endpoints of metallic and insulating behavior, we examine the evolution of a *single* sample under continuous (and reversible, see Fig. S4) tuning of oxygen stoichiometry between these endpoints. Beginning from the state with the highest excess oxygen, stepwise vacuum annealing (see Appendix) reveals a two-stage evolution of transport behavior. In the first stage (Stage I, Fig. 4(a)), the gradual removal of oxygen induces superconductivity from a non-superconducting metallic ground state. Further removal of oxygen (Stage II, Fig. 4(b)) rapidly increases resistivity and eventually drives the system through a superconductor-insulator transition (SIT) [16,17,19], while the resistivity drop at  $T_{c,\text{onset}}$  remains robust. By aligning the  $\rho(T)$  curves of the three LSNO samples in Fig. 3(b) (red, green, and blue) with those of the same sample measured at the beginning and end of Stage I and II in Fig. 4(a)-(b) (also red, green, and blue, respectively), a clear correspondence emerges: the stoichiometric point delineates the crossover between the two stages.

Plotting the conductivity at 200 K,  $\sigma(200\text{ K})$ , against the cumulative annealing time  $t_{\text{anneal}}$  (Fig. 4(d); the  $x$ -axis is reversed so positive  $\delta$  appears on the right) further highlights a distinct crossover separating the two stages:  $\sigma(200\text{ K})$  decreases linearly with  $t_{\text{anneal}}$  in Stage I, but switches to a more rapid, exponential decay in Stage II. Since  $\Delta\delta(t_{\text{anneal}}) \sim \exp(-\lambda t_{\text{anneal}})$  under surface-exchange-limited first-order kinetics [33,34],  $t_{\text{anneal}}$  serves as a smooth, monotonic proxy for  $\delta$  (to leading order  $t_{\text{anneal}} \sim -\Delta\delta$ ). Therefore, the two distinct stages observed in the transport evolution and  $\sigma(200\text{ K})$  with  $t_{\text{anneal}}$  can also be directly mapped to the evolution with  $\delta$ . Interestingly, the intersection of the two fitting functions for each stage in Fig. 4(d) coincides with the

maximum RRR as a function of  $t_{\text{anneal}}$  shown in Fig. 4(c), offering a further indication of the mechanism governing the crossover.

A superconducting half-dome is clearly visible in the resistivity contour (Fig. 4(e)) and in the corresponding derivative contour (Fig. S5), where the  $x$ - and  $y$ -axis represent reversed  $t_{\text{anneal}}$  (as a proxy for  $\delta$ ) and temperature, respectively. The extracted  $T_{c,\text{onset}}$  and  $T_{c,50\%}$  are overlaid on the contours. We use the term half-dome to indicate that on the oxygen-rich side both  $T_{c,\text{onset}}$  and  $T_{c,50\%}$  decrease in tandem, whereas on the oxygen-deficient side  $T_{c,\text{onset}}$  remains nearly unchanged while  $T_{c,50\%}$  collapses approaching the insulating state. The measurement with the highest  $T_{c,10\%}$  (as a proxy for global phase coherence) across all annealing steps is marked as ‘optimized’. We discuss the structure of this superconducting phase diagram in more detail below.

In Stage I ( $\delta > 0$ ), as  $\delta$  increases from stoichiometric ( $\delta \approx 0$ ), the right sector of the superconductivity half-dome evolves in a manner reminiscent of overdoped cuprates [35], where both  $T_{c,\text{onset}}$  and  $T_{c,50\%}$  decrease, shifting in parallel toward zero temperature while maintaining a similar transition width (from green to red curves in Fig. 4(a), see also Fig. 4(e)). When the excess oxygens occupy the interstitial sites between the rock-salt layers [24,25,31], their primary effect is to dope the adjacent  $\text{NiO}_2$  bilayers through a ‘modulation doping’ mechanism—analogueous to doping by interstitial oxygen in BSCCO [35,36]. This is supported by the Drude-like linear increase of  $\sigma(200\text{ K})$  with increasing  $\delta$  (Fig. 4(d)). There is in addition (weak) disorder, evidenced by the slight decrease in RRR with increasing  $\delta$  (Fig. 4(c), also mentioned earlier when discussing Fig. 2(b)-(c)).

In Stage II ( $\delta < 0$ ), as  $\delta$  decreases from near stoichiometric ( $\delta \approx 0$ ), apical and/or planar oxygens are removed [21,22], thereby disrupting the structural continuity of the  $\text{NiO}_2$  bilayer as an integral building block. In cuprates, oxygen vacancies within  $\text{CuO}_2$  planes are also known to be highly detrimental to superconductivity, primarily through the introduction of strong disorder [37]. Similar vacancy formation in nickelates is therefore expected to produce comparable deleterious effects. Moreover, vacancies at the apical oxygen sites—which are essential for maintaining interlayer coupling within the bilayer structure—have been proposed to be catastrophic for superconductivity [38,39]. Consistently, we see a rapid increase of resistivity (from green to blue curves in Fig. 4(b)), an exponential decrease of  $\sigma(200\text{ K})$  (Fig. 4(d)), and a fast decrease in RRR (Fig. 4(c)). While  $T_{c,\text{onset}}$  remains constant or even slightly increases,  $T_{c,50\%}$  abruptly drops to zero (Fig. 4(e)), indicative of the onset of granular superconductivity [28]. This ultimately leads to an SIT: finite-size scaling analysis

yields the critical exponents product  $z\nu = 2.5$ , consistent with the quantum percolation model and previous reports [16] (Fig. S6).

In the Crossover region between Stages I and II ( $\delta \approx 0$ ),  $T_c$  remains nearly constant, with a slight increase as oxygen is removed. Due to entropy considerations and potential spatial inhomogeneity, oxygen vacancies likely start forming before all interstitial oxygens are completely removed. The peak in RRR can be naturally interpreted as a balance point where disorder from both oxygen vacancies and interstitial oxygen is minimized; we therefore label this moment as ‘balanced’. Notably, in Fig. 4(c)-(e), the  $t_{\text{anneal}}$  for the ‘balanced’ point lies slightly on the oxygen-rich side of the ‘optimized’ point. This offset can be understood by considering that oxygen vacancies introduce much stronger disorder, such that their influence outweighs the weaker effects of residual interstitial oxygen, effectively shifting the ‘balanced’ point slightly toward the oxygen-rich side.

Additional insight can be found in the evolution of the  $R_H$  with  $t_{\text{anneal}}$  or change of  $\delta$  (Fig. 4(f)). Positive [6,40], near-zero [7,21], and negative [20,23]  $R_H$  values have been observed in superconducting bilayer nickelate thin films. A recent study also explored the evolution of oxygen-deficient regions [17]. Here, by precisely tuning  $\delta$  from excess, to stoichiometric, and finally to a deficient regime, we reproduce all previously reported trends in  $R_H$ —spanning negative to near-zero to positive (see Fig. S7 for detailed comparison with literature). This complete evolution enables us to pinpoint the negative  $R_H$  corresponding to the optimally superconducting (stoichiometric) sample, as also observed in refs. [20,23]. Another notable feature on the  $\delta > 0$  side is that  $R_H$  reaches its negative minimum and then increases, coinciding with the point when reduction of  $T_c$  occurs (but not with the moment of maximum RRR). As discussed below, this minimum is observed during the change of  $\delta$  in bilayer nickelate films with different substitutional doping, which provides a way to quantify the effect of  $\delta$ .

### C. Oxygen stoichiometry tuning in the presence of calcium doping

Cuprates often exhibit similar phase diagrams upon carrier doping, whether achieved through alkaline-earth substitution or interstitial oxygen intercalation, as exemplified by  $\text{La}_{2-x}\text{Sr}_x\text{CuO}_4$  and  $\text{La}_2\text{CuO}_{4+\delta}$  (ref. [41]). An intriguing question is whether this correspondence also holds for bilayer nickelates, and the potential dual contributions to doping from both cation substitution and oxygen stoichiometry [42]. To address this, we performed extensive investigations of the oxygen-stoichiometry-dependent transport properties of  $\text{La}_{2-x}\text{PrCa}_x\text{Ni}_2\text{O}_{7+\delta}$  (LPCNO) with

different Ca doping levels ( $x = 0, 0.165, 0.382$ ,  $\rho(T)$  shown in Fig. S8) and compared them with those of LSNO.

Resistivity contour plots were constructed as in Fig. 4 for each composition (Fig. 5). To enable a meaningful comparison, however,  $t_{\text{anneal}}$  is not a suitable variable, as both the oxygen loss rate and absolute resistivity are composition and sample dependent, respectively. To address this, two normalization procedures were applied. (i) To compensate for differences in oxygen loss rates among samples,  $\sigma(200\text{ K})$  was used as a monotonic proxy for  $t_{\text{anneal}}$  (Fig. 4(d)), and thus for  $\delta$ . (ii) To correct for variations in absolute resistivity, previous studies on cuprates with varying oxygen stoichiometry renormalized  $\sigma(200\text{ K})$  with respect to the optimally doped state, which serves as a natural reference point [36,43]. In the present case, however, such a well-defined anchor is absent. Instead, we found that the occurrence of an  $R_H$  minimum during vacuum annealing is a robust and generic feature across all samples. Therefore,  $\sigma(200\text{ K})$  was normalized to its value at the  $R_H$  minimum. This procedure provides a reproducible reference frame for tracking the continuous evolution of transport properties with annealing.

Now we present the contour map of resistivity, normalized to its value at 200 K, for the same LSNO sample from Fig. 4, and three LPCNO samples at different doping levels (Fig. 5(a)-(d)) and the corresponding evolutions of  $R_H$  (Fig. 5(e)-(h)). To frame a more general discussion of the superconducting half-domes, we highlight four key observations in Fig. 5. (i) the superconducting region consistently exhibits a half-dome-like structure as discussed earlier, indicating a similar underlying mechanism across changes in the oxygen stoichiometry. (ii) the superconducting half-domes are less complete in LPCNO than those of LSNO. This is likely because ozone annealing near the phase boundary is less robust for LPCNO, as discussed previously in Fig. 2. Consequently, we reduced the scale of annealing compared to for LSNO, which in turn led to a narrower range of resistivity tuning via changing  $\delta$ . We also note that the smaller ion size of Sm than Pr likely allows for a higher concentration of interstitial oxygens. (iii) the right sector of the half-dome becomes more complete with increasing Ca doping, which is consistent with higher initial hole doping. (iv) although determining the precise stoichiometric point is challenging in this system, we can use the ‘optimized’ (as well as the ‘balanced’) criteria introduced in Fig. 4, as an ansatz for the stoichiometric composition. If this assumption holds, the corresponding ‘optimized’ (‘balanced’) point on  $\sigma(200\text{ K})_{\text{norm}}$  axis should shift toward higher values

with increasing Ca doping, which is indeed what is observed.

#### D. General superconducting half-dome in bilayer nickelates

The above observations imply that the interstitial oxygen plays a role analogous to Ca doping, as increasing either one drives the system towards the right sector of the superconducting half-dome. Given that a doping level of 0.19 holes per Ni in the LPCNO sample almost fully suppresses superconductivity, we infer that  $\delta > 0.19$  in the non-superconducting metallic LSNO film, assuming each interstitial oxygen contributes two holes. This is roughly consistent with the bulk value of  $\delta = 0.23$ , where superconductivity is completely suppressed even under pressure [25]. Beyond this carrier-doping perspective, recent bulk studies have also shown that interstitial oxygen can distort the Ni–O bond angle, potentially suppressing superconductivity [24,25]. A similar mechanism may occur in our films; however, unlike in the bulk, where interstitial oxygen stabilizes an orthorhombic phase even under high pressure, epitaxial strain confines films to the tetragonal phase, with the associated interstitial oxygen occupancy configuration yet to be determined.

Returning to Fig. 1, a general phase diagram of samples with different compositions is plotted against  $\sigma(200\text{ K})_{\text{norm}}$  and temperature.  $T_{c,\text{onset}}$  and the metal-insulator transition temperature ( $T_{\text{ins}}$ , defined as the temperature at which  $\rho(T)$  reaches its minimum in the normal state; see Fig. S8) are displayed for all samples with different compositions. For  $\delta > 0$ ,  $T_{c,\text{onset}}$  of all different compositions collapses onto a common curve, forming the right sector of a superconducting half-dome. This indicates that this part of the half-dome represents a quasi-universal behavior of bilayer nickelates, irrespective of Ca doping. As discussed above, the primary effect of Ca doping is to shift the stoichiometric point rightward in the phase diagram shown in Fig. 1. The collapse of the data also supports the validity of normalizing to  $\sigma(200\text{ K})$ , as it self-consistently indicates that the observed trend change in the Hall channel reflects an underlying generic behavior. We speculate that this feature may correspond either to a Lifshitz transition associated with the Fermi level crossing of the  $\gamma$  band upon hole doping, or to the onset of a structural transition upon oxygen intercalation [25]. The former interpretation appears broadly consistent with the scenario proposed in ref. [44], although the precise correspondence remains to be clarified. On the left side, when  $\delta < 0$ , an SIT emerges, but the critical point varies from sample to sample, reflecting differences in the disorder scale. At fixed  $\sigma(200\text{ K})_{\text{norm}}$ , samples with higher Ca doping show higher  $T_{\text{ins}}$  and lower RRR, both suggesting that

Ca substitution introduces additional disorder (Fig. S8). While the occurrence of the SIT is a general feature, the critical  $\sigma(200\text{ K})_{\text{norm}}$  that triggers the SIT is thus sample-dependent.

### III. DISCUSSION

Overall, the robust half-dome-like evolution of  $T_c$  points to an intrinsic asymmetry in the underlying physics, where oxygen interstitials predominantly act as dopants, whereas oxygen vacancies introduce strong disorder. This pronounced sensitivity of superconductivity to vacancies reflects the fact that the inner apical and planar oxygen sites mediate strong Ni–O hybridization and interlayer coupling within the bilayer. Their removal simultaneously reconstructs the relevant  $e_g$  orbital and generates strong local disorder, both of which are highly detrimental to superconducting coherence [38,39].

As for the phase competing with superconductivity in this regime, a natural candidate is a spin-density-wave (SDW) state [45–47]. Oxygen vacancies can play two roles: they decrease the effective Ni valance and introduce quenched randomness along the in-plane Ni–O network. These effects suggest at least two possible routes toward understanding the observed granularity of superconductivity. First, neglecting quenched disorder, an decrease in Ni valance may favor higher-spin states via a larger effective moment [48], thereby stabilizing competing SDW order that suppresses superconductivity. In such a picture, superconductivity may nucleate in isolated regions where magnetic order is locally suppressed, for example near magnetic domain walls [49,50]. Global superconducting coherence would then arise from Josephson tunneling through metallic SDW regions separating superconducting puddles. Second, when quenched randomness and bond disorder are included, the granularity is further enhanced by a rounding of the first-order transition between superconductivity and SDW order with disorder-induced coexistence of both phases [51]. Moreover, quenched disorder drives the metallic SDW electrons toward Anderson localization, weakening Josephson coupling between spatially separated superconducting regions [52,53].

More broadly, this phenomenology bears a conceptual resemblance to longstanding perspectives in cuprates [54], where the underdoped regime is often associated with disorder-dominated or granular superconductivity [55]. In such pictures, superconducting pairing may persist locally even as global phase coherence is limited by inhomogeneity and scattering. The similarity of this framework to the oxygen-deficient regime of bilayer nickelates points to a possible commonality in how disorder, reduced carrier mobility, and phase fluctuations shape

superconducting behavior in oxides. Beyond nickelates and cuprates, analogous behavior has been reported across diverse superconducting systems, including Pb–Ag alloys [28], (Ba,K)BiO<sub>3</sub> (ref. [56]), Li<sub>x</sub>ZrNCl (ref. [57]), and (Li,Fe)OHFeSe (ref. [58]). This suggests that asymmetric superconducting evolution driven by the interplay of doping, disorder, and competing phases is a broader organizing principle across superconductors. A final noteworthy point is the continued increase of  $T_{c,onset}$  toward the insulating regime on the left side of the phase diagram (Fig. S5). This suggests that if electron doping could be achieved in bilayer nickelates without introducing significant disorder, an even higher  $T_c$  might be attainable. In this context, the synthesis of nickelates with new structural motifs represents a promising pathway toward this objective [59].

## APPENDIX: METHODS

### 1. Sample preparation and XRD characterization

The SrLaAlO<sub>4</sub>(001) [SLAO(001)] substrates (MTI Corporation) were sonicated in acetone and IPA for 1 minute each prior to both PLD and MBE growth. For PLD growth, polycrystalline LSNO and LPNO were used as targets during the deposition process. The LSNO and LPNO films were deposited by PLD with a KrF excimer laser (wavelength 248 nm). During the growth, the substrate temperature was maintained at 660 °C under oxygen partial pressure  $p(O_2)$  of 150 mTorr. The pulsed laser repetition rate during the deposition was 5 Hz. The laser fluence was 0.56 J/cm<sup>2</sup> with a spot size of 3.3 mm<sup>2</sup>. For MBE growth, the SLAO substrate was first annealed in 5×10<sup>-6</sup> Torr ozone at 750 °C for 10 minutes. LPNO and LPCNO thin films were then deposited layer by layer at 680 °C in 1.8×10<sup>-6</sup> Torr ozone in a shutter-controlled mode. During growth, reflection high-energy electron diffraction with a 15 keV electron beam was employed to monitor the growth process and film quality. Unlike previous works [6,23], here we do not use a surface capping layer to facilitate oxygen tuning. For both PLD and MBE grown samples, XRD data were measured using a monochromated Cu  $K\alpha 1$  source ( $\lambda = 1.5406$  Å) after growth.

### 2. XAS measurements

XAS experiments were carried out at  $T = 13.5$  K at Beamline 13-3 of the SSRL. The absorption spectra were acquired in total electron-yield mode, with the  $\sigma$ -polarized X-rays incident at 10-degree grazing angle. To preserve oxygen stoichiometry, we adopted the procedures described in [23] during sample storage and transportation.

### 3. Transport measurements

Au electrodes (40 nm thick) were deposited using

electron beam evaporation and then electrodes were bonded to ceramic chip carriers with aluminum wires by an ultrasonic wire bonder before performing ozone annealing. During ozone annealing, electrical transport was measured inside a tube furnace [23]. Low-temperature magnetotransport measurements were performed using <sup>4</sup>He cryostats. The vacuum annealing was then performed within the same <sup>4</sup>He cryostats by raising the temperature to ~360 K and held at that temperature ( $t_{anneal}$ ) before subsequent low-temperature measurements.

### 4. EELS measurements

To prepare cross-sectional scanning transmission electron microscopy (STEM) specimens, we used an FEI Strata 400S focused ion beam (FIB) system with a Quorum PP3010T cryo-stage. The FIB specimen stage was cooled to -192 °C while performing a cryogenic lift-out protocol adapted from ref. [60]. EELS of the O- $K$  edge was measured on the cryo-FIB prepared lamella using a FEI Titan Themis operated at 300 kV accelerating voltage and 21.4 mrad semi-convergence angle equipped with a Gatan Quantum 965 energy filter and a K2 Summit direct electron detector. A Gatan Model 626 cryo-transfer holder was used to maintain specimen temperature below -180 °C throughout the measurement. Keeping the sample cool during FIB process and STEM-EELS measurements preserves oxygen stoichiometry which is altered if performed at room temperature. Spectra were recorded with an energy dispersion of 0.1 eV per channel, 0.7 Å spatial step size, 3710 energy channels, and a 75 pA probe current.

### ACKNOWLEDGEMENTS

We thank W. He, S. A. Kivelson, Y. S. Lee, R. Peng, H. C. Xu, and Y. Zhang for discussions and assistance. This work was supported by the US Department of Energy, Office of Basic Energy Sciences, Division of Materials Sciences and Engineering (contract no. DE-AC0276SF00515), as well as the Kavli Foundation, Klaus Tschira Stiftung, and Kevin Wells (development of in-situ annealing). Work at the Stanford Nano Shared Facilities (SNSF) RRID:SCR\_023230 is supported by the National Science Foundation under grant ECCS-1542152. B.H.G. was supported by the Max Planck Society. L.B. and D.A.M. acknowledge support by the NSF Platform for the Accelerated Realization, Analysis, and Discovery of Interface Materials (PARADIM) under cooperative agreement No. DMR-2039380. B.H.G. was supported by the Max Planck Society. STEM related work made use of the Cornell Center for Materials Research shared instrumentation facility. The FEI Titan Themis 300 was acquired through NSF-MRI-1429155, with additional support from Cornell

University, the Weill Institute, and the Kavli Institute at Cornell. Support for the FIB/SEM cryo-stage and transfer system was provided by the Kavli Institute at Cornell and the Energy Materials Center at Cornell, DOE EFRC BES (DE-SC0001086). X-ray measurements were carried out at the SSRL, SLAC National Accelerator Laboratory, supported by the US Department of Energy, Office of Science, Office of Basic Energy Sciences (contract no. DE-AC02-76SF00515).

#### AUTHOR CONTRIBUTIONS

Y.L. and B.Y.W. contributed equally to this work. Y.Y., H.Y.H. and Z.-X.S. supervised this project. B.Y.W., Y.L., H.Y.H., and Y.Y. conceived and designed the study. Y.L. synthesized LSNO and LPNO films, and B.Y.W. synthesized LPNO and LPCNO films. Y.Y., Y.L. and Y.T. studied the ozone annealing effects. Y.Y., Y.L., and B.Y.W. characterized and studied the transport properties with the assistance of Y.T. L.B., M.C., B.H.G. and D.A.M. performed EELS studies. J.L. performed the XAS measurements with support from C.T.K. and J.S.L. All experimental contributions of Y.Y. were performed at Stanford. Y.L., B.Y.W., J.L., Y.-M.W., S.R., H.Y.H. and Y.Y. analyzed the data. Y.L., B.Y.W., S.R., H.Y.H. and Y.Y. wrote the paper with input from all authors.

#### DATA AVAILABILITY

The data presented in the figures and other findings of this study are available from the corresponding authors upon reasonable request.

- 
- [1] D. J. Scalapino, *A common thread: The pairing interaction for unconventional superconductors*, Rev. Mod. Phys. **84**, 1383 (2012).
- [2] B. Keimer, S. A. Kivelson, M. R. Norman, S. Uchida, and J. Zaanen, *From quantum matter to high-temperature superconductivity in copper oxides*, Nature **518**, 179 (2015).
- [3] H. Sun et al., *Signatures of superconductivity near 80 K in a nickelate under high pressure*, Nature **621**, 493 (2023).
- [4] J. Hou et al., *Emergence of High-Temperature Superconducting Phase in Pressurized  $\text{La}_3\text{Ni}_2\text{O}_7$  Crystals*, Chin. Phys. Lett. **40**, 117302 (2023).
- [5] Y. Zhang et al., *High-temperature superconductivity with zero resistance and strange-metal behaviour in  $\text{La}_3\text{Ni}_2\text{O}_{7-\delta}$* , Nat. Phys. **20**, 1269 (2024).
- [6] E. K. Ko et al., *Signatures of ambient pressure superconductivity in thin film  $\text{La}_3\text{Ni}_2\text{O}_7$* , Nature **638**, 935 (2025).
- [7] G. Zhou et al., *Ambient-pressure superconductivity onset above 40 K in  $(\text{La},\text{Pr})_3\text{Ni}_2\text{O}_7$  films*, Nature **640**, 641 (2025).
- [8] G. Wang et al., *Pressure-Induced Superconductivity In Polycrystalline  $\text{La}_3\text{Ni}_2\text{O}_{7-\delta}$* , Phys. Rev. X **14**, 011040 (2024).
- [9] J. Li et al., *Identification of superconductivity in bilayer nickelate  $\text{La}_3\text{Ni}_2\text{O}_7$  under high pressure up to 100 GPa*, Natl. Sci. Rev. **12**, nwaf220 (2025).
- [10] N. Wang et al., *Bulk high-temperature superconductivity in pressurized tetragonal  $\text{La}_2\text{PrNi}_2\text{O}_7$* , Nature **634**, 579 (2024).
- [11] F. Li et al., *Bulk superconductivity up to 96 K in pressurized nickelate single crystals*, Nature **649**, 871 (2025).
- [12] T. Cui et al., *Strain-mediated phase crossover in Ruddlesden–Popper nickelates*, Commun. Mater. **5**, 32 (2024).
- [13] L. Bhatt et al., *Resolving Structural Origins for Superconductivity in Strain-Engineered  $\text{La}_3\text{Ni}_2\text{O}_7$  Thin Films*, arXiv:2501.08204.
- [14] M. Osada, C. Terakura, A. Kikkawa, M. Nakajima, H.-Y. Chen, Y. Nomura, Y. Tokura, and A. Tsukazaki, *Strain-tuning for superconductivity in  $\text{La}_3\text{Ni}_2\text{O}_7$  thin films*, Commun. Phys. **8**, 251 (2025).
- [15] Y. Tarn et al., *Reducing the Strain Required for Ambient-Pressure Superconductivity in Ruddlesden–Popper Bilayer Nickelates*, Adv. Mater. e20724 (2026).
- [16] H. Wang et al., *Electronic Structures across the Superconductor–Insulator Transition at  $\text{La}_{2.85}\text{Pr}_{0.15}\text{Ni}_2\text{O}_7/\text{SrLaAlO}_4$  Interfaces*.
- [17] M. Wang, B. Hao, W. Sun, S. Yan, S. Sun, H. Zhang, Z. Gu, and Y. Nie, *Superconducting Dome in  $\text{La}_{3-x}\text{Sr}_x\text{Ni}_2\text{O}_{7-\delta}$  Thin Films*, Phys. Rev. Lett. **136**, 066002 (2026).
- [18] Y. Ueki, H. Sakurai, H. Nagata, K. Yamane, R. Matsumoto, K. Terashima, K. Hirose, H. Ohta, M. Kato, and Y. Takano, *Phase Diagram of Pressure-Induced High Temperature Superconductor  $\text{La}_3\text{Ni}_2\text{O}_{7+\delta}$* , J. Phys. Soc. Jpn. **94**, 013703 (2025).
- [19] L. Xiang, S. Lei, X. Ren, Z. Han, Z. Xu, X. J. Zhou, and Z. Zhu, *Stabilizing and Tuning Superconductivity in  $\text{La}_3\text{Ni}_2\text{O}_{7-\delta}$  Films: Oxygen Recycling Protocol Reveals Hole-Doping Analogue*, arXiv:2508.11581.
- [20] Y. Shi et al., *Critical Thickness and Long-Term Ambient Stability in Superconducting  $\text{LaPr}_2\text{Ni}_2\text{O}_7$  Films*, Adv. Mater. e10394 (2025).
- [21] B. Hao et al., *Superconductivity in Sr-doped  $\text{La}_3\text{Ni}_2\text{O}_7$  thin films*, Nat. Mater. **24**, 1756 (2025).
- [22] Z. Dong et al., *Visualization of oxygen vacancies and self-doped ligand holes in  $\text{La}_3\text{Ni}_2\text{O}_{7-\delta}$* ,

- Nature **630**, 847 (2024).
- [23] Y. Liu et al., *Superconductivity and normal-state transport in compressively strained  $\text{La}_2\text{PrNi}_2\text{O}_7$  thin films*, Nat. Mater. **24**, 1221 (2025).
- [24] X. Chen, N. Wang, Q. Zhang, B. Wang, G. Wang, B. Wang, J. Cheng, and L. Gu, *Interlayer Switching of  $\text{NiO}_6$  Octahedra Tilt via Interstitial Oxygen in  $\text{La}_{n+1}\text{Ni}_n\text{O}_{3n+1}$  ( $n = 1, 2, 3$ )*, Adv. Mater. **37**, e04238 (2025).
- [25] Z. Dong, G. Wang, N. Wang, W.-H. Dong, L. Gu, Y. Xu, J. Cheng, Z. Chen, and Y. Wang, *Interstitial oxygen order and its competition with superconductivity in  $\text{La}_2\text{PrNi}_2\text{O}_{7+\delta}$* , Nat. Mater. **24**, 1927 (2025).
- [26] Y. Zhang et al., *Strong oxidizing annealing of bilayer  $\text{La}_3\text{Ni}_2\text{O}_{7-\delta}$  results in suppression of superconductivity under high pressure*, J. Solid State Chem. **355**, 125757 (2026).
- [27] M. Shi et al., *Spin density wave rather than tetragonal structure is prerequisite for superconductivity in  $\text{La}_3\text{Ni}_2\text{O}_{7-\delta}$* , Nat. Commun. **16**, 9141 (2025).
- [28] L. Merchant, J. Ostrick, R. P. Barber, and R. C. Dynes, *Crossover from phase fluctuation to amplitude-dominated superconductivity: A model system*, Phys. Rev. B **63**, 134508 (2001).
- [29] J. M. Tranquada, Y. Kong, J. E. Lorenzo, D. J. Buttrey, D. E. Rice, and V. Sachan, *Oxygen intercalation, stage ordering, and phase separation in  $\text{La}_2\text{NiO}_{4+\delta}$  with  $0.05 \lesssim \delta \lesssim 0.11$* , Phys. Rev. B **50**, 6340 (1994).
- [30] Z. Zhang, M. Greenblatt, and J. B. Goodenough, *Synthesis, Structure, and Properties of the Layered Perovskite  $\text{La}_3\text{Ni}_2\text{O}_{7-\delta}$* , J. Solid State Chem. **108**, 402 (1994).
- [31] D. Ferenc Segedin et al., *Topochemical Oxidation of Ruddlesden–Popper Nickelates Reveals Distinct Structural Family: Oxygen-Intercalated Layered Perovskites*, J. Am. Chem. Soc. jacs.5c12712 (2026).
- [32] M. R. Presland, J. L. Tallon, R. G. Buckley, R. S. Liu, and N. E. Flower, *General trends in oxygen stoichiometry effects on  $T_c$  in Bi and Tl superconductors*, Phys. C **176**, 95 (1991).
- [33] M. W. Den Otter, H. J. M. Bouwmeester, B. A. Boukamp, and H. Verweij, *Reactor Flush Time Correction in Relaxation Experiments*, J. Electrochem. Soc. **148**, J1 (2001).
- [34] J. A. Kilner and M. Burriel, *Materials for Intermediate-Temperature Solid-Oxide Fuel Cells*, Annu. Rev. Mater. Res. **44**, 365 (2014).
- [35] E. Sterpetti, J. Biscaras, A. Erb, and A. Shukla, *Comprehensive phase diagram of two-dimensional space charge doped  $\text{Bi}_2\text{Sr}_2\text{CaCu}_2\text{O}_{8+x}$* , Nat. Commun. **8**, 2060 (2017).
- [36] Y. Yu, L. Ma, P. Cai, R. Zhong, C. Ye, J. Shen, G. D. Gu, X. H. Chen, and Y. Zhang, *High-temperature superconductivity in monolayer  $\text{Bi}_2\text{Sr}_2\text{CaCu}_2\text{O}_{8+\delta}$* , Nature **575**, 156 (2019).
- [37] I. Zeljkovic, Z. Xu, J. Wen, G. Gu, R. S. Markiewicz, and J. E. Hoffman, *Imaging the Impact of Single Oxygen Atoms on Superconducting  $\text{Bi}_{2+y}\text{Sr}_{2-y}\text{CaCu}_2\text{O}_{8+x}$* , Science **337**, 320 (2012).
- [38] Y.-B. Liu, J.-W. Mei, F. Ye, W.-Q. Chen, and F. Yang,  *$s\pm$ -Wave Pairing and the Destructive Role of Apical-Oxygen Deficiencies in  $\text{La}_3\text{Ni}_2\text{O}_7$  under Pressure*, Phys. Rev. Lett. **131**, 236002 (2023).
- [39] X. Sui, X. Han, H. Jin, X. Chen, L. Qiao, X. Shao, and B. Huang, *Electronic properties of the bilayer nickelates  $\text{R}_3\text{Ni}_2\text{O}_7$  with oxygen vacancies ( $\text{R}=\text{La}$  or  $\text{Ce}$ )*, Phys. Rev. B **109**, 205156 (2024).
- [40] Q. Li et al., *Enhanced superconductivity in the compressively strained bilayer nickelate thin films by pressure*, Nat. Commun. (2026).
- [41] B. O. Wells, Y. S. Lee, M. A. Kastner, R. J. Christianson, R. J. Birgeneau, K. Yamada, Y. Endoh, and G. Shirane, *Incommensurate Spin Fluctuations in High-Transition Temperature Superconductors*, Science **277**, 1067 (1997).
- [42] J. L. Tallon, C. Bernhard, H. Shaked, R. L. Hitterman, and J. D. Jorgensen, *Generic superconducting phase behavior in high- $T_c$  cuprates:  $T_c$  variation with hole concentration in  $\text{YBa}_2\text{Cu}_3\text{O}_{7-\delta}$* , Phys. Rev. B **51**, 12911 (1995).
- [43] A. T. Bollinger, G. Dubuis, J. Yoon, D. Pavuna, J. Misewich, and I. Božović, *Superconductor–insulator transition in  $\text{La}_{2-x}\text{Sr}_x\text{CuO}_4$  at the pair quantum resistance*, Nature **472**, 458 (2011).
- [44] S. Ryee, N. Witt, G. Sangiovanni, and T. O. Wehling, *Superconductivity Governed by Janus-Faced Fermiology in Strained Bilayer Nickelates*, Phys. Rev. Lett. **135**, 236003 (2025).
- [45] D. Zhao, Y. Zhou, M. Huo, Y. Wang, L. Nie, Y. Yang, J. Ying, M. Wang, T. Wu, and X. Chen, *Pressure-enhanced spin-density-wave transition in double-layer nickelate  $\text{La}_3\text{Ni}_2\text{O}_{7-\delta}$* , Sci. Bull. **70**, 1239 (2025).
- [46] T. Xie et al., *Strong interlayer magnetic exchange coupling in  $\text{La}_3\text{Ni}_2\text{O}_{7-\delta}$  revealed by inelastic neutron scattering*, Sci. Bull. **69**, 3221 (2024).
- [47] X. Chen et al., *Electronic and magnetic excitations in  $\text{La}_3\text{Ni}_2\text{O}_7$* , Nat. Commun. **15**, 9597 (2024).
- [48] H. Oh, Y.-M. Wu, J. May-Mann, Y. Yu, H. Y. Hwang, Y.-H. Zhang, and S. Raghu, *High spin, low spin, or gapped spins: Magnetism in the bilayer nickelates*, Phys. Rev. B **113**, 024430 (2026).

- [49] S. A. Kivelson, G. Aeppli, and V. J. Emery, *Thermodynamics of the interplay between magnetism and high-temperature superconductivity*, Proc. Natl. Acad. Sci. U.S.A. **98**, 11903 (2001).
- [50] S. A. Kivelson, D.-H. Lee, E. Fradkin, and V. Oganesyan, *Competing order in the mixed state of high-temperature superconductors*, Phys. Rev. B **66**, 144516 (2002).
- [51] H. Ji et al., *Time-Reversal Symmetry Breaking Superconductivity with Electronic Glass in Nickelate (La, Pr, Sm)<sub>3</sub>Ni<sub>2</sub>O<sub>7</sub> Films*, arXiv:2508.16412.
- [52] Y. Imry and M. Strongin, *Destruction of superconductivity in granular and highly disordered metals*, Phys. Rev. B **24**, 6353 (1981).
- [53] M. V. Feigel'man, L. B. Ioffe, V. E. Kravtsov, and E. Cuevas, *Fractal superconductivity near localization threshold*, Ann. Phys. (N. Y.) **325**, 1390 (2010).
- [54] V. J. Emery, S. A. Kivelson, and O. Zachar, *Spin-gap proximity effect mechanism of high-temperature superconductivity*, Phys. Rev. B **56**, 6120 (1997).
- [55] K. M. Lang, V. Madhavan, J. E. Hoffman, E. W. Hudson, H. Eisaki, S. Uchida, and J. C. Davis, *Imaging the granular structure of high- $T_c$  superconductivity in underdoped  $\text{Bi}_2\text{Sr}_2\text{CaCu}_2\text{O}_{8+\delta}$* , (2002).
- [56] Y. Nagata, A. Mishiro, T. Uchida, M. Ohtsuka, and H. Samata, *Normal-state transport properties of  $\text{Ba}_{1-x}\text{K}_x\text{BiO}_2$  crystals*, J. Phys. Chem. Solids **60**, 1933 (1999).
- [57] Y. Nakagawa, Y. Kasahara, T. Nomoto, R. Arita, T. Nojima, and Y. Iwasa, *Gate-controlled BCS-BEC crossover in a two-dimensional superconductor*, Science **372**, 190 (2021).
- [58] B. Lei et al., *Gate-tuned superconductor-insulator transition in (Li,Fe)OHFeSe*, Phys. Rev. B **93**, 060501 (2016).
- [59] R. Wernert, R. D. Smyth, and M. A. Hayward, *Synthesis of the Double Infinite-Layer Ni(I) Phase  $\text{La}_3\text{Ni}_2\text{O}_5\text{F}$  via Sequential Topochemical Reactions*, J. Am. Chem. Soc. jacs.5c16740 (2026).
- [60] M. J. Zachman, Z. Tu, S. Choudhury, L. A. Archer, and L. F. Kourkoutis, *Cryo-STEM mapping of solid-liquid interfaces and dendrites in lithium-metal batteries*, Nature **560**, 345 (2018).
- [61] L. Wang et al., *Spontaneous phase segregation of  $\text{Sr}_2\text{NiO}_3$  and  $\text{SrNi}_2\text{O}_3$  during  $\text{SrNiO}_3$  heteroepitaxy*, Sci. Adv. **7**, eabe2866 (2021).

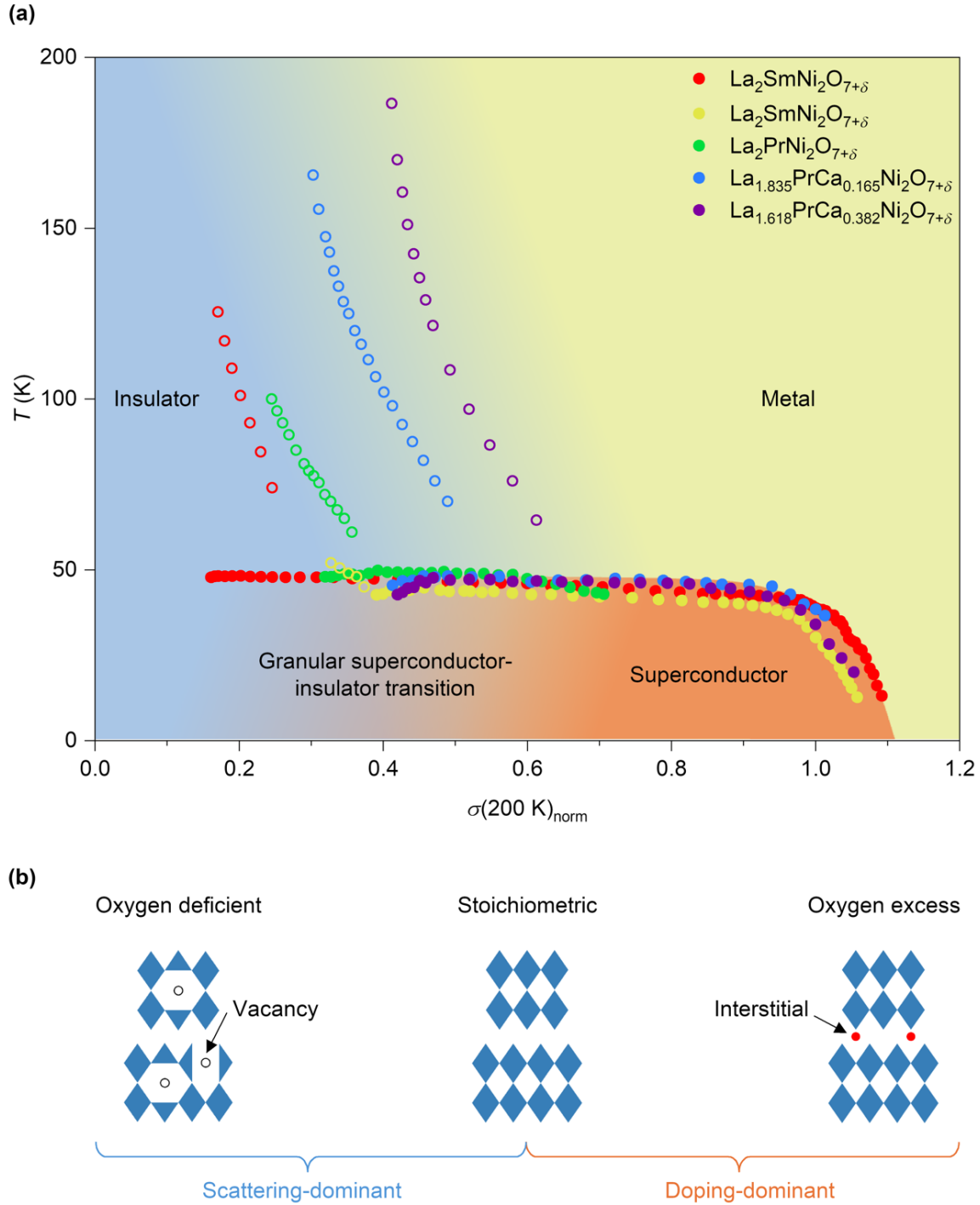


FIG. 1. Superconducting phase diagram of bilayer nickelate films. (a) General phase diagram plotted against  $T$  and  $\sigma(200\text{ K})_{\text{norm}}$  obtained from samples studied in this work. Here,  $\sigma(200\text{ K})_{\text{norm}}$ , defined in the main text, serves as a proxy for oxygen stoichiometry, with oxygen content increasing from left (deficient) to right (excess).  $T_{c,\text{onset}}$  and  $T_{\text{ins}}$  are labeled with filled and open circles. As the oxygen content increases from the deficient regime toward stoichiometry, a granular superconducting phase emerges from the insulator (blue), followed by the establishment of a robust superconducting state (red). Further oxygen incorporation beyond stoichiometry suppresses superconductivity, and the ground state evolves to a metal (yellow). Notably, granular superconductivity emerges exclusively on the oxygen-deficient side, giving rise to a half-dome-like structure. (b) Schematic of the structural evolution under varying oxygen stoichiometry. The contrasting roles of scattering versus doping are indicated.

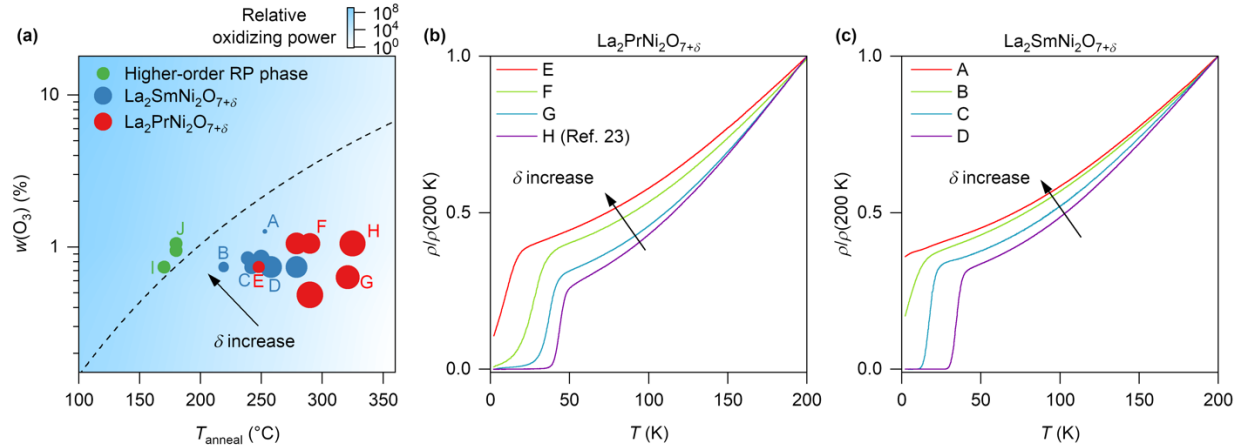


FIG. 2. Superconductivity of bilayer nickelate thin films under different ozone annealing conditions. (a) Phase diagram of ozone annealing temperature  $T_{\text{anneal}}$  vs. ozone concentration  $w(\text{O}_3)$ . Filled green circles represent films transformed into higher-order RP phases, while blue and red dots correspond to LSNO and LPNO films remaining in the bilayer phase. The size of each blue and red dot reflects the  $T_{c,\text{onset}}$  of each sample. The black dashed line represents the estimated stability boundary from ref. [23], above which the bilayer phase cannot be maintained; approaching this boundary allows more oxygen insertion. (b)-(c)  $\rho(T)$  normalized at 200 K for LPNO and LSNO under different ozone annealing conditions, respectively. Both  $T_{c,\text{onset}}$  and the normal-state resistivity evolve systematically with annealing conditions. Each curve corresponds to a sample labeled with the same letter as in (a).

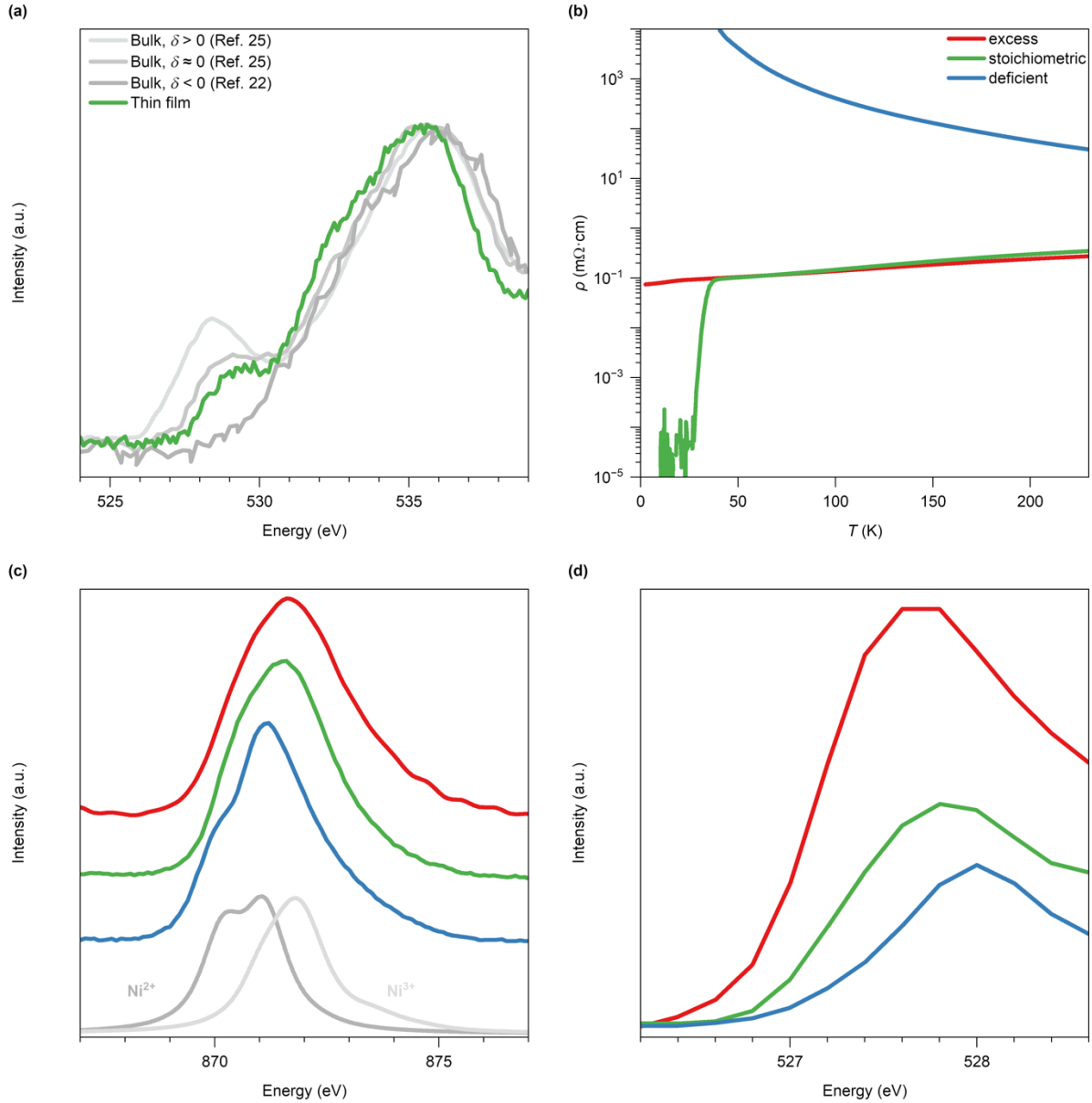


FIG. 3. Spectroscopic benchmarking of oxygen stoichiometry in bilayer nickelate thin films. (a) O  $K$ -edge EELS spectra of LPNO thin film sample with optimal superconductivity. Light grey, grey, and dark grey curves are reference spectra of bulk LPNO with positive, near zero, and negative  $\delta$  from refs. [22,25]. (b)  $\rho(T)$  of three LSNO thin film samples: as-grown (labeled 'deficient'), metallic after ozone annealing (labeled 'excess'), and with optimal superconductivity after ozone annealing (labeled 'stoichiometric'). (c) Ni  $L_2$ -edge XAS spectra of the same samples in (b). Dark and light grey lines are reference spectra for  $\text{Ni}^{2+}$  and  $\text{Ni}^{3+}$  from refs. [47,61]. (d) O  $K$ -edge XAS spectra of the same samples in (b).

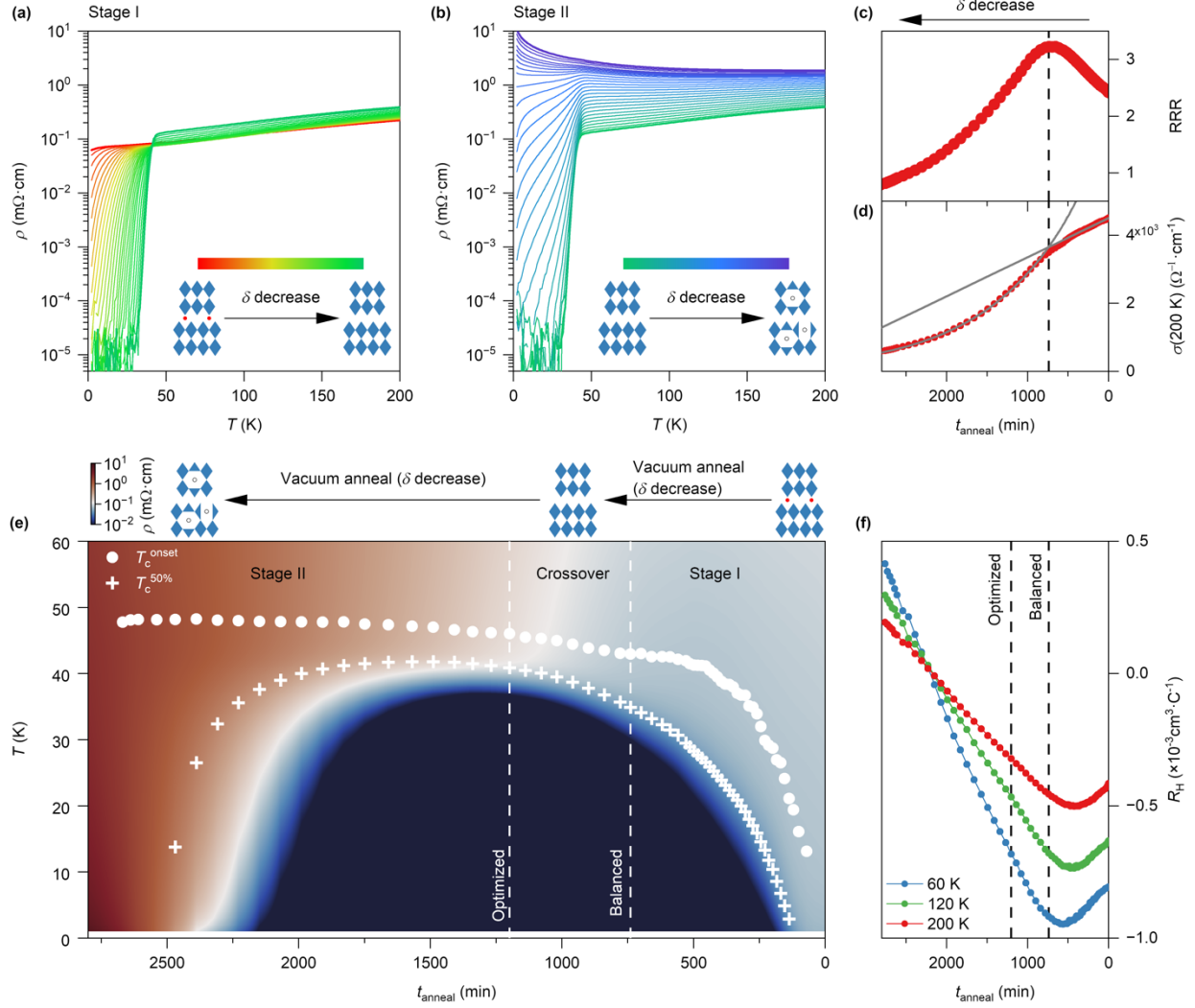


FIG. 4. A superconducting half-dome tuned by oxygen stoichiometry in an LSNO thin film. (a)-(b)  $\rho(T)$  of an ozone-annealed LSNO thin film sample measured after sequential vacuum annealing. (a) shows the evolution from the metallic state to optimized superconductivity (Stage I and Crossover), while (b) shows further evolution from optimized superconductivity to the insulating state (Crossover and Stage II). (c)-(d) Evolution of RRR and  $\sigma(200\text{ K})$  plotted against  $t_{\text{anneal}}$ , respectively. In (d), the grey curves indicate the fitted results using different functionals corresponding to Stages I and II for  $\sigma(200\text{ K})$ , respectively. The vertical dashed line aligns the intersection of two fittings in (d) and coincides with the maximum of RRR in (c). (e) Contour map of  $\rho$  plot against  $T$  and  $t_{\text{anneal}}$ , showing a superconducting half-dome. The inset schematics in (a), (b), and (e) sketch the structural evolution under oxygen stoichiometry change. The dashed lines indicate the positions for ‘optimized’ and ‘balanced’ states, with the Crossover region defined between them. (f) Evolution of  $R_H$  at 60, 120, and 200 K plotted against  $t_{\text{anneal}}$ . The dashed lines indicate the positions for ‘optimized’ and ‘balanced’ states.

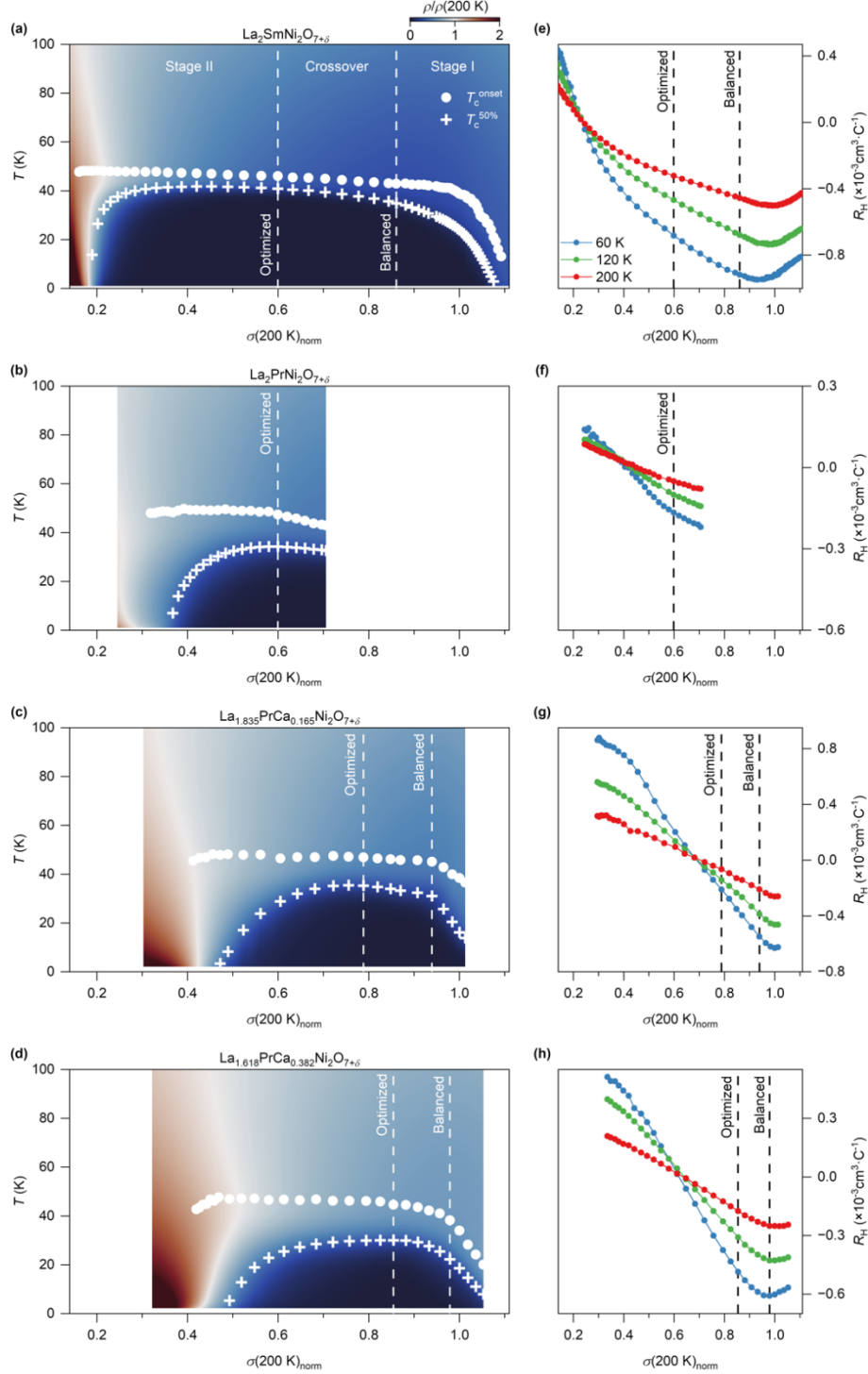


FIG. 5. Superconducting half-domes in LSNO and LPCNO films. (a) Contour maps of  $\rho/\rho(200\text{ K})$  plotted against  $T$  and  $\sigma(200\text{ K})_{\text{norm}}$  of the same sample in Fig. 4. (b)-(d) Contour maps of  $\rho/\rho(200\text{ K})$  plotted against  $T$  and  $\sigma(200\text{ K})_{\text{norm}}$  of LPCNO thin films with  $x = 0, 0.165, 0.382$ , respectively. Each shows a similar but incomplete half-dome-like contour as in (a). (e)-(h) Evolution of  $R_H$  at 60, 120, and 200 K plotted against  $\sigma(200\text{ K})_{\text{norm}}$  for the same samples in (a)-(d), respectively. All exhibit similar trends, with slight variations in the magnitude of  $R_H$  among samples. The dashed lines indicate the positions of ‘optimized’ and ‘balanced’ states for each sample.  $\sigma(200\text{ K})$  in (b) is scaled such that the point corresponding to optimized superconductivity aligns with that of LSNO in (a), as no local minimum is observed in  $R_H$ . Since no well-defined maximum in RRR is observed in (b), the ‘balanced’ position is not labeled.

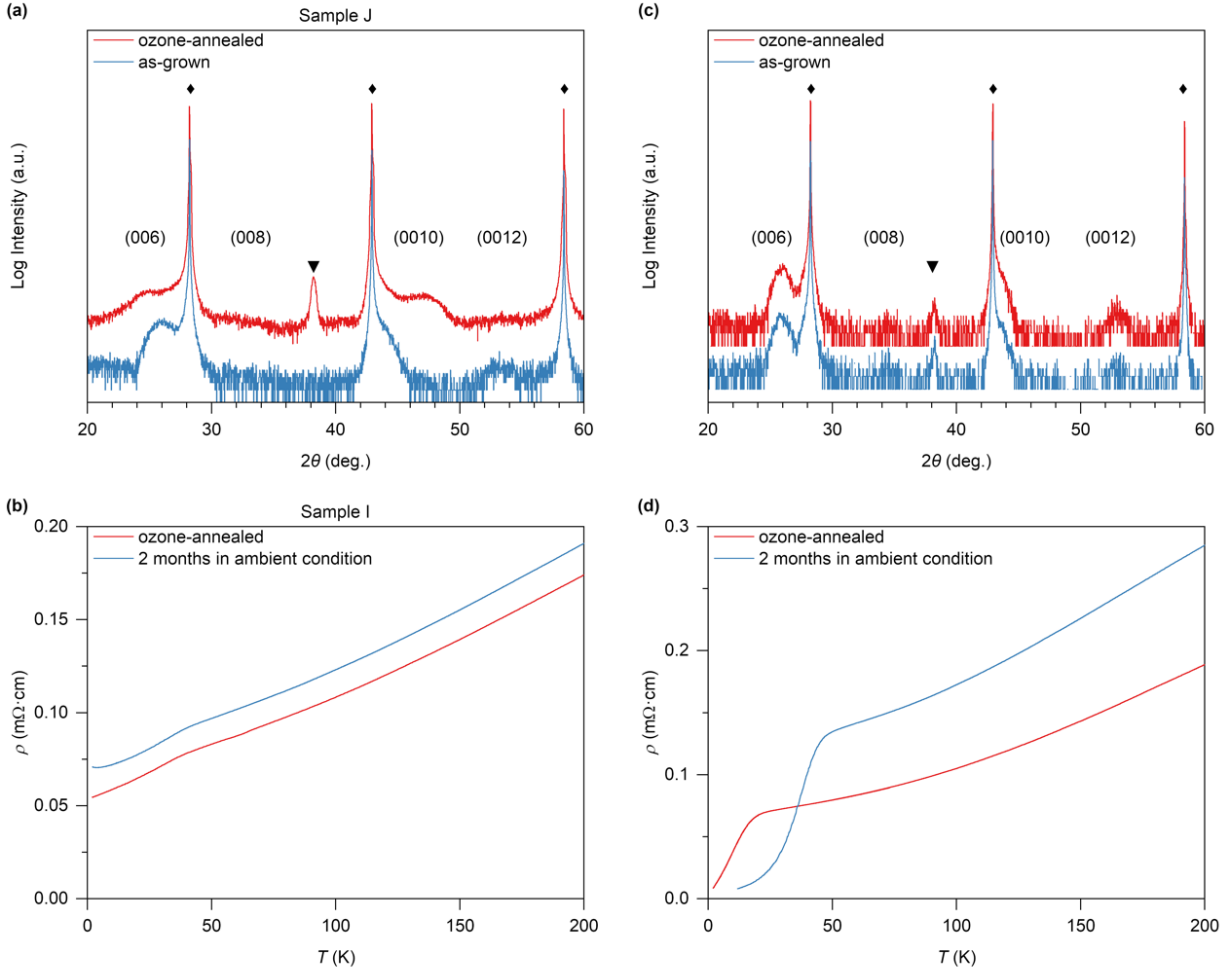


FIG. S1. Transport and structural evolution of bilayer nickelate thin films under different ozone annealing conditions. (a), (c) XRD  $\theta$ - $2\theta$  symmetric scans of LPNO thin film samples (labeled as sample I and J in Fig. 2(a), respectively) before and after ozone annealing. In (a), aggressive ozone annealing triggers the transformation to mixed higher-order RP phases, while in (c), the bilayer structure is preserved but with excess oxygen. The SLAO(001) substrate peaks are marked by  $\blacklozenge$ . The gold (111) peak is marked by  $\blacktriangledown$ . (b), (d)  $\rho(T)$  of LPNO thin film samples measured after ozone annealing and subsequently after two months in ambient conditions. If the material is (partially) transformed into higher-order RP phases (a), superconductivity remains absent after oxygen loss (b). In contrast, for samples in which the bilayer structure is preserved (c),  $T_c$  is enhanced upon oxygen loss (d).

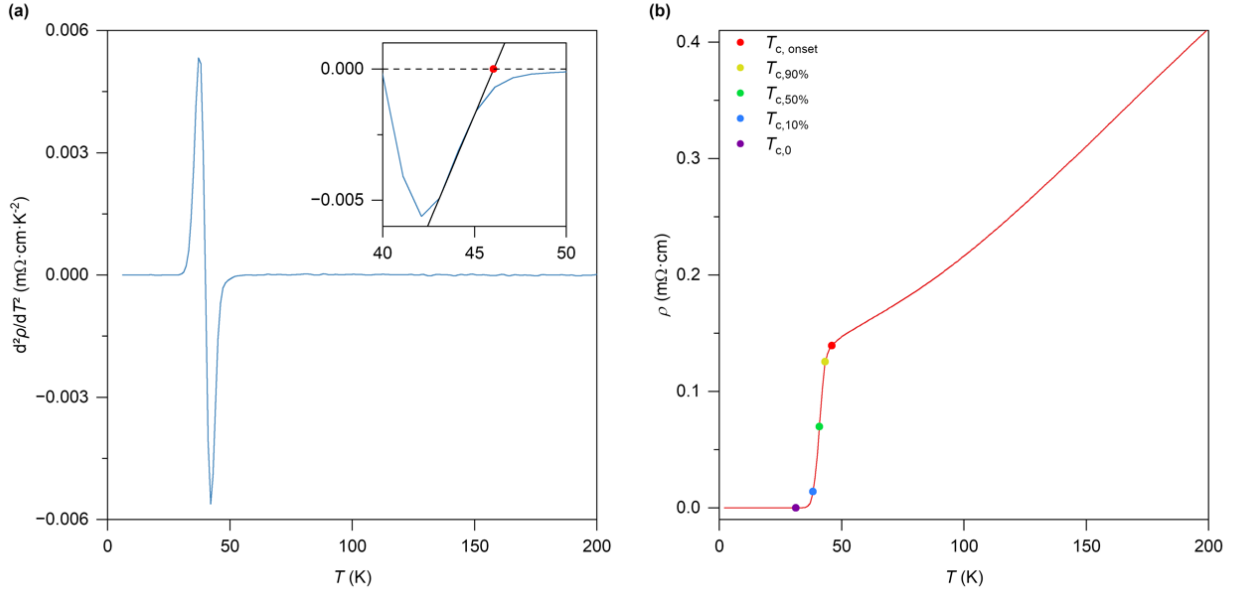


FIG. S2. Definition of transition temperatures. (a)  $d^2\rho/dT^2$  of an optimally superconducting LSNO thin film sample. Inset:  $T_{c,\text{onset}}$  is obtained by linearly fitting to the approximately linear region near the onset of the transition, with the zero intercept of the fit defining  $T_{c,\text{onset}}$ . (b)  $\rho(T)$  of the sample in (a). The red, yellow, green, blue, and purple filled circles represent  $T_{c,\text{onset}}$ ,  $T_{c,90\%}$ ,  $T_{c,50\%}$ ,  $T_{c,10\%}$ , and  $T_{c,0}$ , respectively.  $T_{c,90\%}$ ,  $T_{c,50\%}$ , and  $T_{c,10\%}$  are defined as the temperatures where the resistance reaches 90%, 50%, and 10% of the normal-state resistance near  $T_{c,\text{onset}}$ .

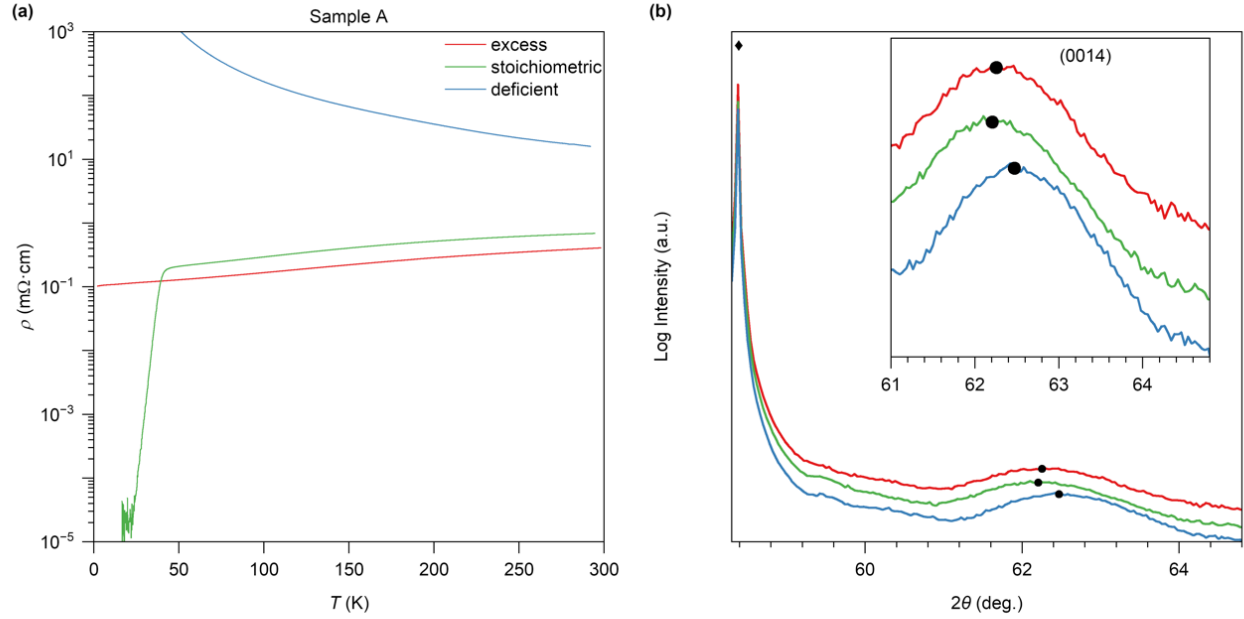


FIG. S3. Evolution of XRD patterns of bilayer nickelate thin films with different oxygen stoichiometries. (a)  $\rho(T)$  of one LSNO thin film sample (labeled as sample A in Fig. 2(a)), measured after sequential post-growth treatments: as-grown (labeled ‘deficient’), after ozone annealing to a metallic state (labeled ‘excess’), and after vacuum-annealing to optimal superconductivity (labeled ‘stoichiometric’). (b) XRD  $\theta$ - $2\theta$  symmetric scans of LSNO sample after each step of post-growth treatments. The SLAO(001) substrate peaks are marked by  $\blacklozenge$ , and the (0014) peaks of LSNO are marked by  $\bullet$ . The inset zooms in on the (0014) film peak. A  $c$  lattice expansion is observed as the samples evolve from an oxygen-deficient insulating state to a stoichiometric optimally superconducting state, consistent with ref. [18]. Subsequently, a very slight contraction is observed upon transitioning to the oxygen-excess metallic state, consistent with recent bulk reports [18,25]. However, the evolution of  $c$  lattice with oxygen stoichiometry is not consistent across different literature studies. For instance, contrary to our observation, a bulk report suggested that slightly oxygen-deficient samples possess a larger  $c$  lattice than stoichiometric ones [30]. Additionally, another report on thin films has shown a pronounced  $c$  lattice expansion, rather than contraction, upon intercalating interstitial oxygen [31]. These discrepancies likely stem from multiple factors. The presence of polymorphism and mixed RP phases in early studies hinders exact stoichiometry determination in bulk, and variations in structural symmetry with oxygen content complicate lattice analysis [26,31]. Moreover, the epitaxial strain in thin films likely induces different structural responses to oxygen stoichiometry compared to bulk.

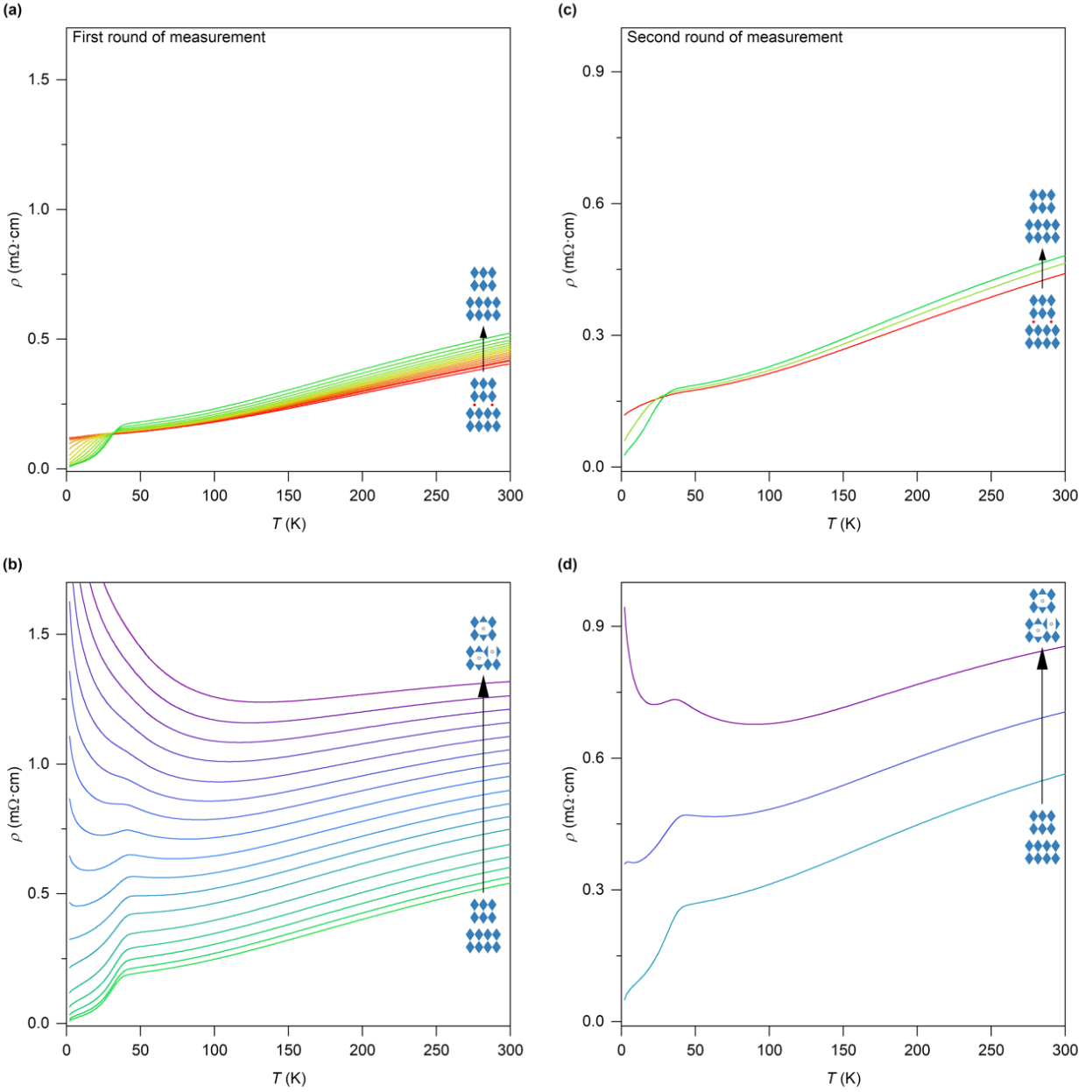


FIG. S4. Reversibility of continuous oxygen tuning. (a)-(d)  $\rho(T)$  of LPNO thin films subjected to a first and second cycle of ozone annealing, measured after sequential vacuum annealing. (a), (c) show the evolution from the metallic state to the superconducting state (Stage I to Crossover), while (b), (d) show further evolution from the superconducting state to the insulating state (Crossover to Stage II). (a)-(b) correspond to the first-round ozone-annealed sample while (c)-(d) represent the second-round ozone-annealed sample. The inset schematics illustrate the structural response to changes in oxygen stoichiometry. Although the crystallinity somewhat degraded after the second ozone annealing, a similar evolution in transport properties was observed in both measurement rounds.

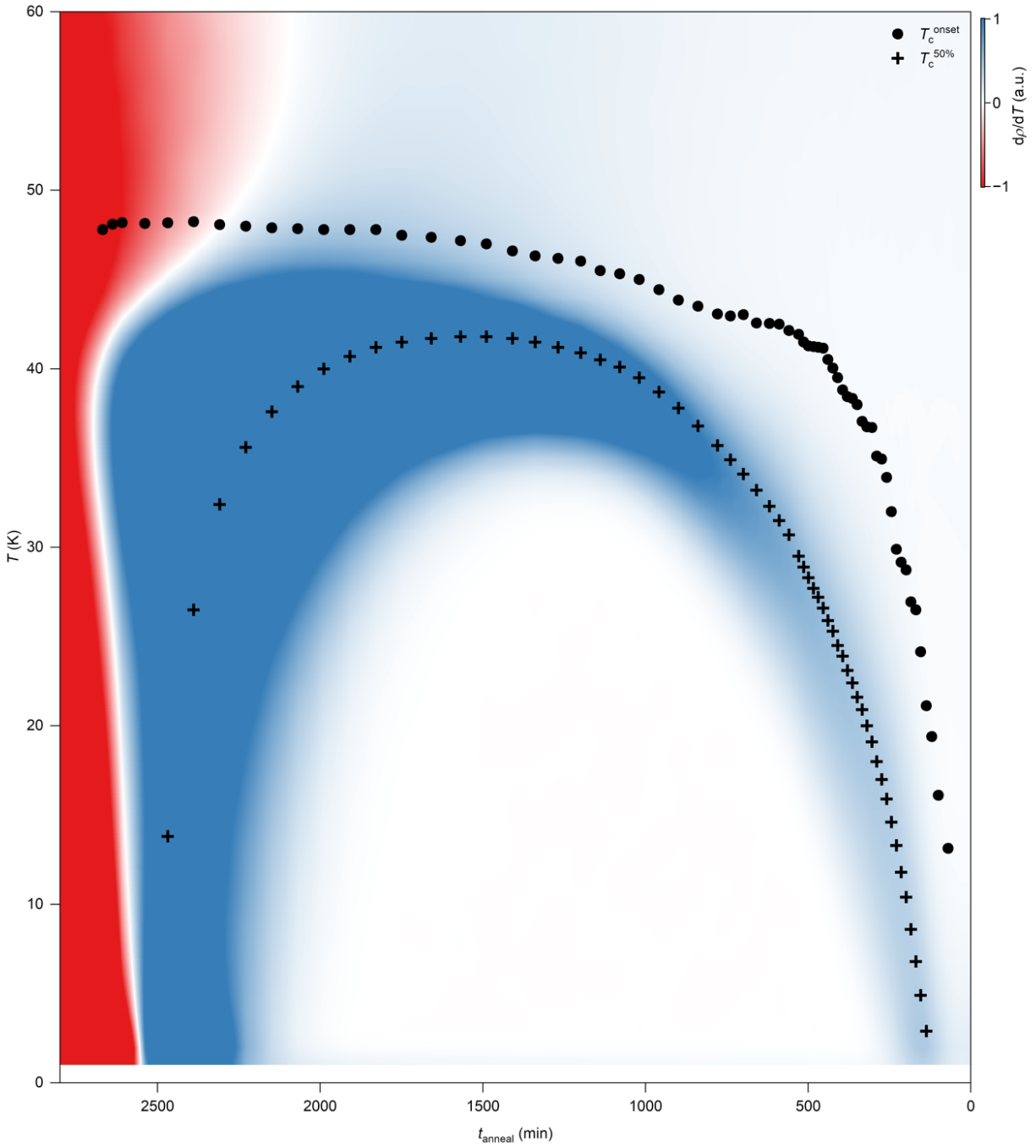


FIG. S5. A superconducting half-dome tuned by oxygen stoichiometry in an LSNO thin film. Contour map of  $d\rho/dT$  plotted against  $T$  and  $t_{\text{anneal}}$ , where blue and red regions represent positive and negative  $d\rho/dT$ , indicating the presence of superconducting and insulating transitions, respectively. On the right side, the superconducting transition width—indicated by the extent of the blue region—remains nearly constant, whereas on the left, the transition broadens rapidly as  $T_{c,50\%}$  collapses with decreasing  $\delta$ .

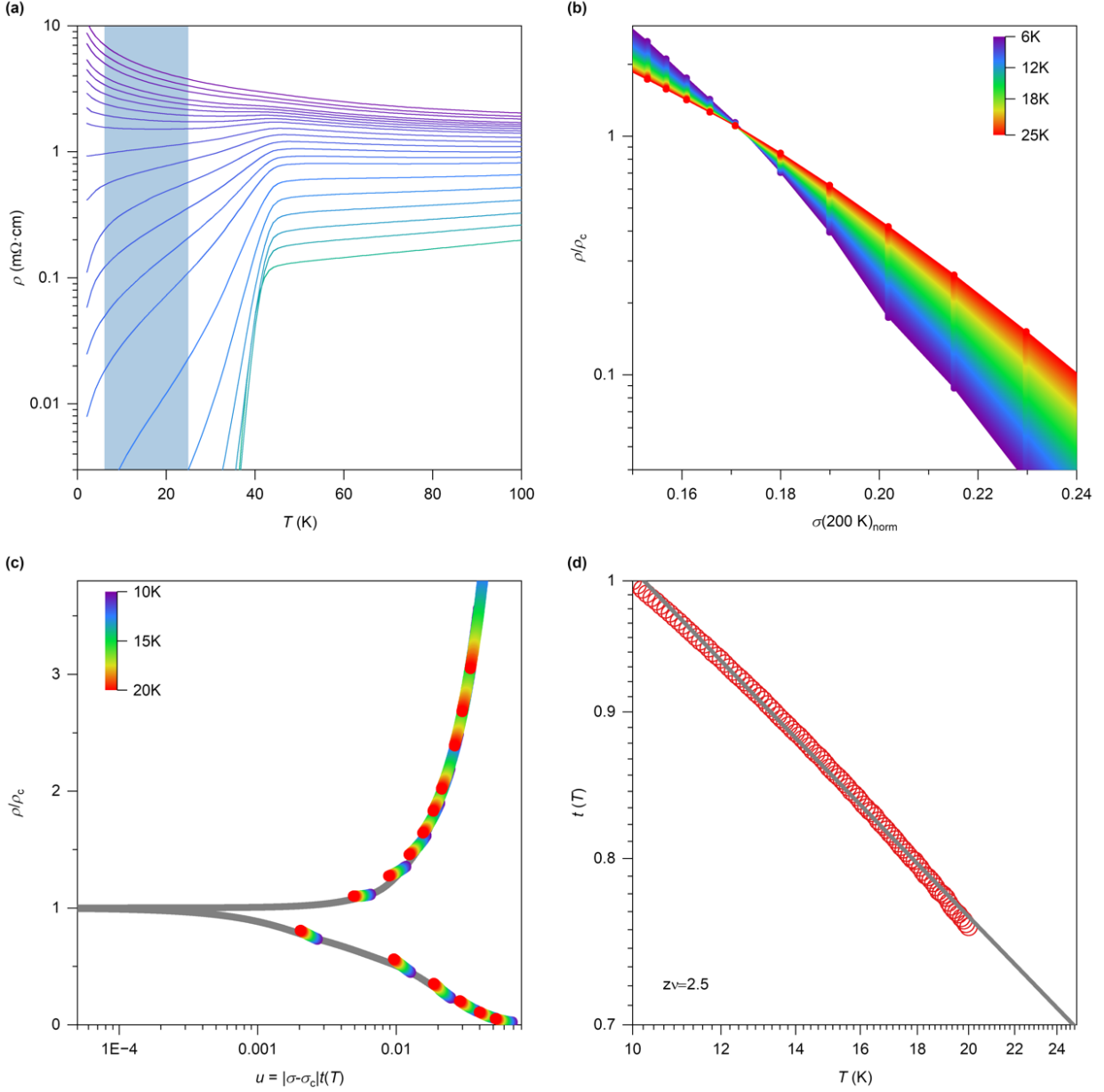


FIG. S6. Scaling analysis of the SIT in bilayer nickelate thin films. (a)  $\rho(T)$  of ozone-annealed LSNO thin films measured after sequential vacuum annealing in Stage II (the same sample shown in Fig. 4). The blue shaded region shows the temperature range for the finite-size scaling analysis. (b) The same dataset in (a) plotted as a function of doping level at fixed temperatures between 6 K and 25 K, with each color representing a fixed temperature. Continuous curves are interpolations of data points at different temperatures. All curves cross at the critical resistance  $\rho_c = 13.8$  k $\Omega$ /bilayer. (c) Scaling of the same data with respect to variable  $u = |\sigma - \sigma_c|t(T)$ . A single set of temperature-dependent parameters  $t(T)$  can collapse all data to a universal scaling function on both sides of the SIT. (d)  $t(T)$  obtained from finite-size scaling analysis in (c). The slope of the line fit (grey line) yields the critical exponents product  $z\nu = 2.5$ .

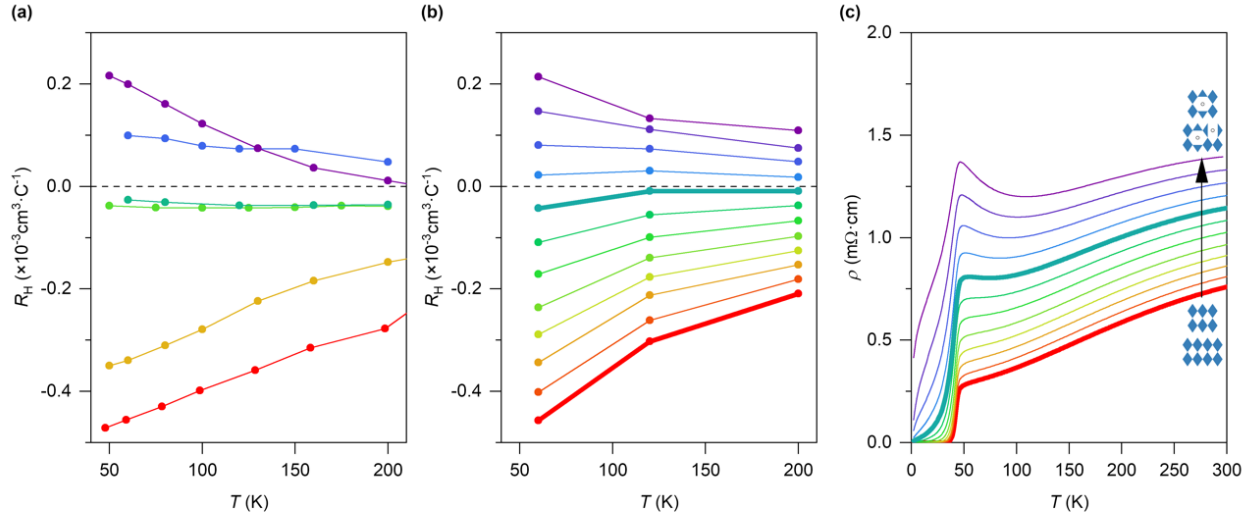


FIG. S7. Evolution of the Hall coefficient with temperature ( $R_H(T)$ ) in bilayer nickelate thin films with different oxygen stoichiometries. (a)  $R_H(T)$  data from refs. [6,40,7,21,23,20] (ordered top to bottom). (b)  $R_H(T)$  for the sample shown in Fig. 4, where colors denote different oxygen stoichiometries. (c)  $\rho(T)$  of the same sample as in (b) at various oxygen stoichiometries. Curves corresponding to the same stoichiometry share the same color. The schematic on the right illustrates the structural changes associated with varying oxygen stoichiometry.

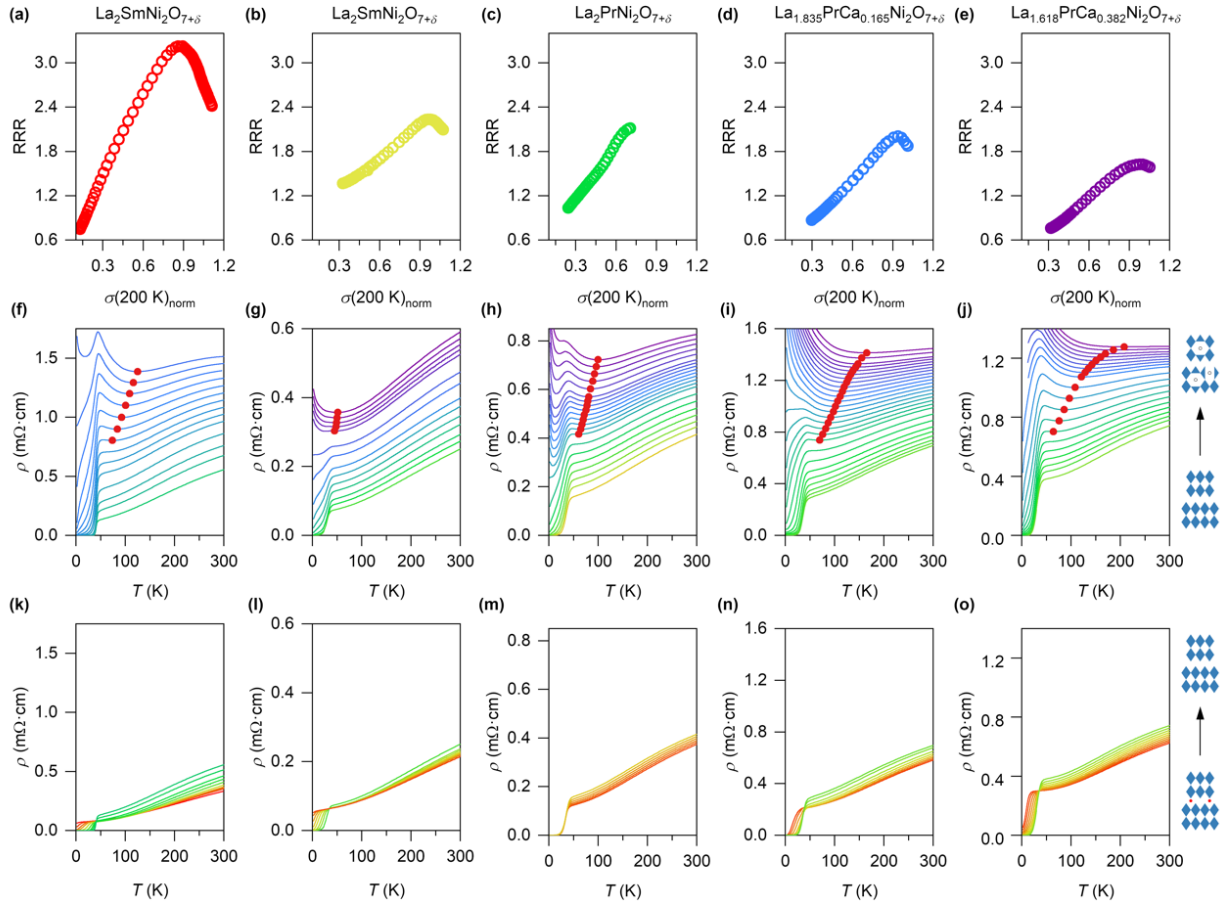


FIG. S8. Evolution of transport properties in bilayer nickelate thin films with different oxygen stoichiometries. (a)-(e) Evolution of RRR plotted against  $\sigma(200\text{ K})_{\text{norm}}$  for the same samples shown in Fig. 1. Each curve corresponds to the sample with the same color as in Fig. 1. (f)-(o) Selected  $\rho(T)$  for the same samples as in (a)-(e). (k)-(o) show the evolution from the metallic state to optimal superconductivity (Stage I to Crossover), respectively. (f)-(j) show further evolution from the optimally superconducting state to the insulating state (Crossover to Stage II), respectively.  $T_{\text{ins}}$  indicated by filled red circles. The schematics on the right illustrate the structural evolution driven by changes in oxygen stoichiometry.